Computers, Materials & Continua

Tech Science Press

https://doi.org/10.32604/cmc.2026.084077

ARTICLE

Parametric Characteristics Analysis of Three-Unit-Cell Model in 3D Seven-Directional Braided Composites

Xiyue Zhang[1], Feizhou Li[1,*], Zhihai Hu[1], Weiliang Zhang[1], Xindang He[2], Gexia Yuan[1], Yanwei Feng[3] and Yafeng Qi[4,5,*]

[1]Institute of Mechanical Engineering, Baoji University of Arts and Sciences, Baoji, China
[2]Department of Mechanics, Civil Engineering and Architecture, Northwestern Polytechnical University, Xi'an, China
[3]College of Electron-Mechanics and Automobile Engineering, Tianshui Normal University, Tianshui, China
[4]State Key Laboratory of Electromechanical Integrated Manufacturing of High-Performance Electronic Equipment, School of Electro-Mechanical Engineering, Xidian University, Xi'an, China
[5]State Key Laboratory of Tribology in Advanced Equipment, Tsinghua University, Beijing, China

*Corresponding Authors: Feizhou Li. Email: lfz-1010@163.com; Yafeng Qi. Email: qi6279@126.com

Received: 16 April 2026; Accepted: 25 June 2026; Published: 13 August 2026

ABSTRACT: Three-dimensional (3D) braided composites are widely used in aerospace and automotive industries due to their superior mechanical properties. However, traditional 3D four-directional or five-directional braided composites exhibit limitations in multi-axial load-bearing capacity and structural stability under complex stress conditions. To address these challenges, we propose a novel 3D seven-directional braided composite structure, which enhances mechanical performance in both axial and transverse directions by incorporating additional reinforcement yarns. This structure consists of braiding yarns, axial yarns, six-directional yarns and seven-directional yarns, forming a more uniform and stable interlacing network. Based on the positional relationships between yarns, a parametric three-unit-cell model (incorporating interior, surface, and corner unit-cells) was developed to analyze the effects of braiding parameters and angles on fiber volume fraction and unit-cell geometry. Especially, an automated modeling plugin was created to efficiently generate unit-cell models for further mechanical analysis. The proposed 3D seven-directional braided composite provides a new theoretical framework for designing advanced textile composites, expanding their potential for diverse engineering applications.

KEYWORDS: 3D seven-directional braided composites; braiding parameters; fiber volume fraction; three-unit-cell model

1 Introduction

3D braided composites have attracted extensive attention due to their unique 3D braided structure. Through the continuous interweaving of fibers in space, this material exhibits excellent mechanical properties such as high strength [1], high modulus [2], and good impact resistance [3], while overcoming the defect of low interlaminar strength in traditional two-dimensional composites [4–6]. In addition, its good thermal stability and strong designability endow it with broad application prospects in aerospace, automotive industry, marine engineering, medical devices and other fields [7–10].

With the continuous improvement of application requirements, especially in the scenarios of complex multi-directional loads [11] and high-temperature environments [12], the performance of 3D braided composites has been given higher demands. However, the performance of braided composites is significantly affected by the braiding angle and volume fraction [13–15]. In order to optimize its performance, it is necessary to construct a large number of unit-cell models to find the optimal combination of braiding parameters. In addition, due to the complex yarn structure of braided composites, realizing rapid modeling [16–18] is crucial to accelerate its application and development.

The research on mesoscopic scale models of 3D braided composites has evolved from the early simplified models [19–22] that laid the theoretical foundation, to the three-unit-cell model [23,24] and CAD modeling techniques [25,26] that promoted structural characterization. In the 21st century, finite element multiphase models [27–29], fiber volume fraction models [30,31], and studies on the influence of braiding parameters [32–34] have gradually deepened the field. In recent years, the three-unit-cell model for 3D seven-directional braiding [35], the multiscale elastoplastic damage model [36–38], and the virtual braiding technology [39,40] have marked the development of this field towards high-precision digitization.

3D seven-directional braided composites further optimize the yarn arrangement based on traditional 3D four-directional or five-directional braided structures, forming a more complex multi-axial network structure by introducing additional reinforcing yarns (sixth and seventh-directional yarns) [41,42]. This design not only continues the advantages of five-directional braided materials in interlaminar strength, impact resistance, and in-plane performance [43,44], but also significantly enhances the material's mechanical response capability under complex multi-axial loads through the synergistic effect of multi-dimensional yarns [45,46]. However, due to its complex microstructure, few numerical studies have been specifically dedicated to evaluating the performance of 3D seven-directional braided composites. For the widespread application of 3D seven-directional braided composites, it is necessary to develop appropriate models to investigate their mechanical properties and potential damage mechanisms.

This study focuses on the mesoscopic characteristics of 3D seven-directional braided composites and their influence mechanisms on material properties. Specifically, it aims to explore the geometric features of the three-unit-cell model of 3D seven-directional braided composites, the influence laws of braiding parameters such as braiding angles, braiding geometric parameter, and yarn number on unit-cell size, fiber volume fraction, and unit-cell mass, and create a method for rapidly establishing 3D seven-directional unit-cell models. Through the above research, it is intended to solve the problem of insufficient mechanical properties of existing 3D braided composites in complex stress environments and provide a theoretical basis for optimizing material design.

2 Materials and Methods

2.1 The Composition of Yarns

In 3D seven-directional rectangular braiding, the yarns are divided into two groups: the first group is the braided yarns and axial yarns, which are carried by the yarn carriers on the machine chassis; the second group is the vertical six-directional yarns and seven-directional yarns, which are fed one by one between the rows and columns of the yarn carriers. During braiding, the yarn carriers move in a specific sequence to form a rectangular array of p rows and q columns, conforming to the cross-sectional shape of the 3D seven-directional braided preform. The number of braided yarns (N_1) in the square array can be calculated by Eq. (1), and the total number of axial yarns (N_2) can be calculated by Eq. (2). In one braiding cycle, the number of six-directional yarns (N_3) and seven-directional yarns (N_4) can be calculated by Eqs. (3) and (4), respectively.

$$N_1 = pq + p + q \quad (1)$$

$$N_2 = pq \quad (2)$$

$$N_3 = 2(p - 1) \tag{3}$$

$$N_4 = 2(q - 1) \tag{4}$$

2.2 Four-Step Braiding Process and Movement Paths of Yarns

The detailed process of the four-step braiding process is shown in Fig. 1. The circular symbol (°) and the cross symbol (×) represent the carriers of braided yarns and axial yarns, respectively. The purple and red dotted lines represent the movement trajectories of six-directional and seven-directional yarns, respectively. Fig. 1A shows the initial position. In the first step, the even-numbered rows move in the $+X$ direction while the odd-numbered rows move in the $-X$ direction. Once in position, the six-directional yarns (purple dotted trajectories) are synchronously fed to ensure uniform distribution along the row gaps (Fig. 1B). In the second step, the even-numbered column carriers move in the $+Y$ direction and the odd-numbered columns in the $-Y$ direction. Upon reaching their positions, the seven-directional yarns (red dotted trajectories) are fed synchronously to align with the column gaps (Fig. 1C). In the third/fourth steps, the carriers move in reverse directions (Fig. 1D,E), repeating the yarn feeding logic to form a closed-loop synchronization mechanism of "move-feed-reverse move-feed again". This coordinated pattern ensures that the six-directional/seven-directional yarns are each inserted twice per braiding cycle, maintaining a stable phase difference with the carrier displacements.

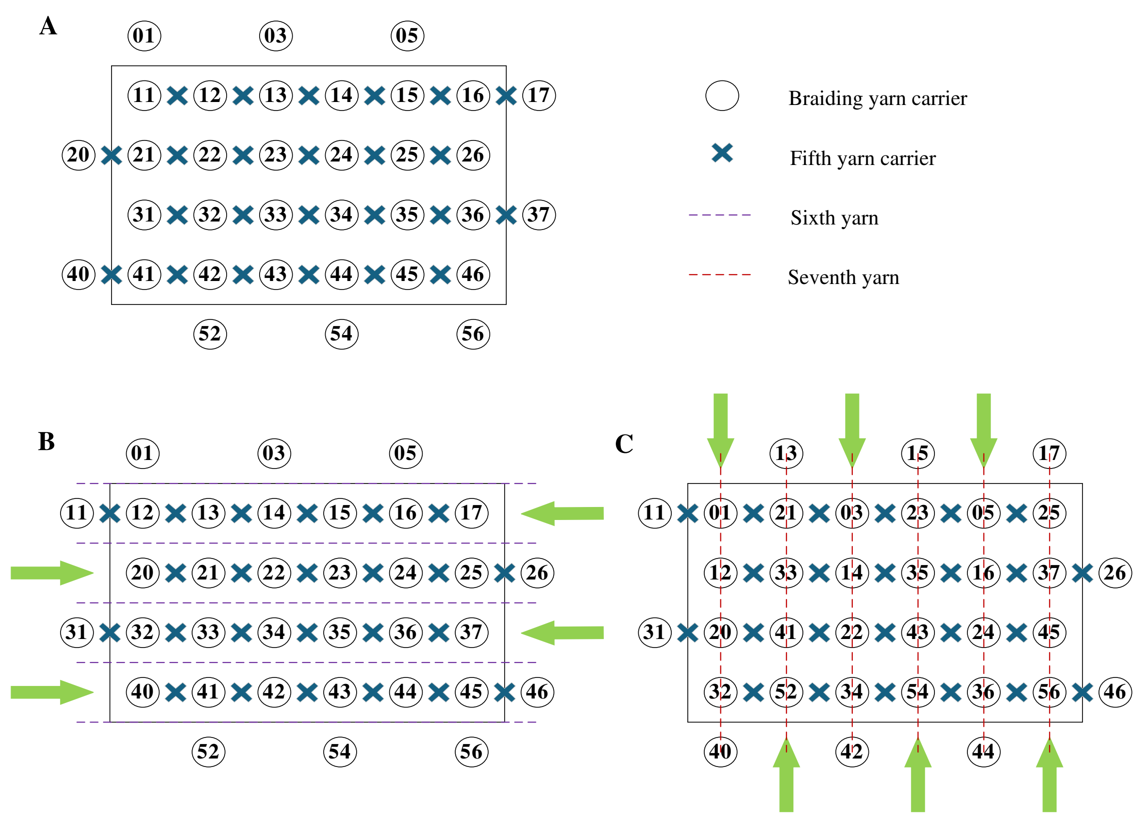

Figure 1: (Continued)

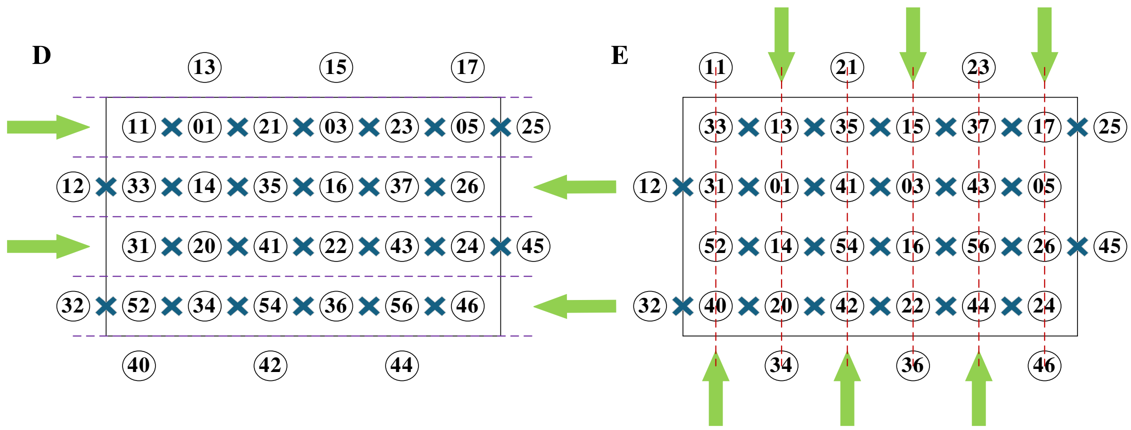

Figure 1: Four-step braiding process of 3D seven-directional braided preform. (**A**), the Initial position. (**B**–**E**), the different position in the four-step braiding process.

The movement paths of yarns in the horizontal plane of the 3D seven-directional braided preform are complex, as shown in Fig. 2 where the parallel oblique straight lines are the movement trajectories of the braided yarns, and the arrows indicate the moving directions. The angle between the movement direction of the internal braided yarns and the thickness direction of the preform is φ. The yarns move back and forth between the interior and the surface. The surface yarn paths adhere to the internal paths. The internal braided yarns present two sets of parallel paths in opposite directions, and the movement trends of adjacent yarns are opposite. The projections of the braided yarns on the plane are represented by "○" and are evenly distributed. The paths of the six-directional yarns are horizontal lines, and the paths of the seven-directional yarns are vertical lines.

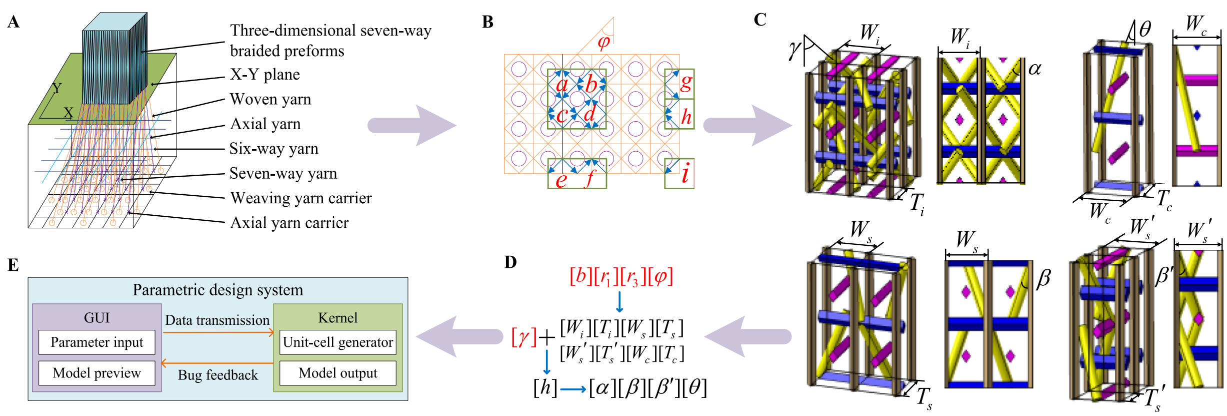

Figure 2: Workflow of parametric modeling and design system for 3D seven-directional braided composites: (**A**) Four-step braiding process of 3D seven-directional preform (**B**) Geometric modeling and parametric characterization of yarn trajectories (**C**) Unit-cell geometric model construction and parametric symbol (**D**) Symbolic derivation of mathematical relationships between parameters (**E**) Architecture and module interaction of the parametric design system.

The movement characteristics of the yarn carriers inside and on the surface of the machine are different. Coupled with the differences in the corner areas of the preform, the interlacing structures of the yarns in each area show diversity. During the braiding process, the yarns are guided by the carriers, moving along the length direction of the preform in each step to form specific spatial paths and unit-cell models, and finally braiding into a preform of a specific length. To improve modeling efficiency, the minimum research unit of the 3D seven-directional rectangular braided composite is divided into three forms, namely the internal unit-cell, the surface unit-cell, and the corner unit-cell [47,48]. As shown in Fig. 2B, the four regions a, b, c and d represent the yarn interlacing structure of the internal unit-cell, the four regions e, f, g and h represent the yarn interlacing structure of the surface unit-cell, and the region i represents the yarn interlacing structure of the corner unit-cell.

2.3 Cross-Sections of Yarns

Fig. 3 shows the cross-sectional shapes of the three types of yarns in 3D seven-direction. The cross-section of the braided yarn is elliptical [49–51]. Half of the major axis of the ellipse is a, and half of the minor axis is b. S_1 is the cross-sectional area of the ellipse, and $S_1 = \pi ab$. The cross-section of the axial yarn is square. The lengths of the diagonals of the square are $2r_1b$, and S_2 is the cross-sectional area of the axial yarn, with $S_2 = 2r_1^2b^2$. The cross-sections of the six-directional and seven-directional yarns are rhombic. The two diagonals of the rhombus are $2r_2b$ and $2r_2b/\tan\alpha$, and S_3 is the cross-sectional area of the six-directional and seven-directional yarns, with $S_3 = 2r_2^2b^2/\tan\alpha$.

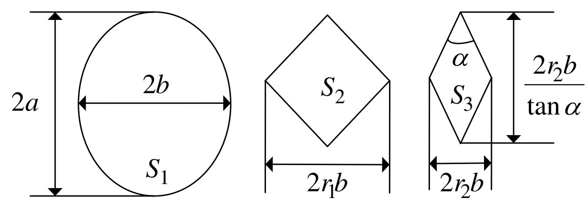

Figure 3: Cross-sections of yarns.

Since the yarn bundle is a micro-scale fiber-reinforced resin composite material, the concept of the fiber packing factor is introduced to represent the volume fraction of fibers in the yarn. The fiber packing factor is equal to the ratio of the equivalent diameter of the fibers to the equivalent cross-sectional area, and can be expressed as:

$$\varepsilon_b = \frac{\pi D_y^2}{4S_1} = \frac{D_y^2}{4ab} \tag{5}$$

$$\varepsilon_{za} = \frac{\pi D_y^2}{4S_2} = \frac{\pi D_y^2}{8r_1^2b^2} \tag{6}$$

$$\varepsilon_{ta} = \frac{\pi D_y^2}{4S_3} = \frac{\pi D_y^2\tan\alpha}{8r_2^2b^2} \tag{7}$$

According to the assumption, different types of yarn bundles need to have the same fiber packing factor, that is $\varepsilon = \varepsilon_b = \varepsilon_{za} = \varepsilon_{ta}$.

2.4 Parametric Calculation of the Internal Unit-Cell

The internal unit-cell structure of the preform is composed of four representative structural units, as shown in Fig. 4A. The internal unit-cell in Fig. 4A is further subdivided into four sub-regions a, b, c and d. The specific yarn interlacing structures are shown in the four sub-figures of Fig. 4C, corresponding to the four regions of the internal unit-cell in Fig. 2B, respectively. These figures reveal how the yarns in different regions are interlaced and arranged according to a specific process at the micro-level of the braided composite, forming four internal sub-cell models.

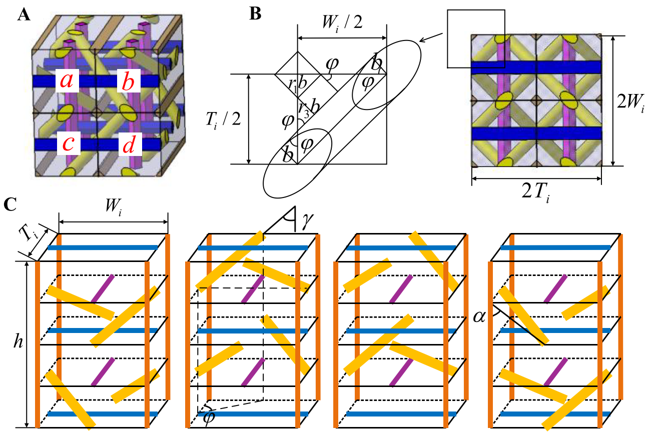

Figure 4: Internal unit-cell structure: 3D model (**A**), OXY projection (**B**) and yarn interweaving details (**C**).

As shown in Fig. 4C, the direction of the internal model is parallel to the surface of the preform. Each internal unit-cell model contains braided yarns in four directions and four quarter axial yarns. The four groups of braided yarns are placed in two intersecting parallel planes, and are distributed as $+\gamma$ and $-\gamma$, respectively in each adjacent parallel plane. The axial yarns are similar to the braiding direction and are distributed at the four corners. In addition, the six-directional and seven-directional yarns are evenly distributed on two different horizontal planes, perpendicular to the braiding direction.

Considering the tightening process of the yarns during the braiding process, the relationship between the major semi-axis a and the minor semi-axis b can be calculated by means of spatial geometric relationships:

$$a = b\sqrt{3}\cos\gamma \tag{8}$$

According to the planar geometric relationships in Fig. 4B, the dimensions of the internal unit-cell can be obtained as follows:

$$W_i = \frac{2(1+r_3)b}{\cos\varphi} + 2r_1b \tag{9}$$

$$T_i = \frac{2(1+r_3)b}{\sin\varphi} + 2r_1b \tag{10}$$

$$\tan\alpha = \frac{2W_i}{h} = \frac{4(1+r_3)b}{h\cos\varphi} + \frac{4r_1b}{h} \tag{11}$$

$$h = \frac{2W_i}{\sin\varphi\tan\gamma} = \frac{8(1+r_3)b}{\sin 2\varphi\tan\gamma} + \frac{4r_1b}{\sin\varphi\tan\gamma} = \frac{8(1+r_3)b + 8r_1b\cos\varphi}{\sin 2\varphi\tan\gamma} \tag{12}$$

2.5 Parametric Calculation of the Surface Unit-Cell

The surface unit-cell structure of the preform comprises four representative structural units (Fig. 5A,C), with the width-direction and thickness-direction surface unit-cells further subdivided into sub-regions e, f and g, h, respectively. The specific yarn interlacing structures are shown in the four sub-figures of Fig. 5E,F, corresponding to the four regions of the surface unit-cell in Fig. 2B, respectively. The direction of the surface unit-cell model is parallel to the surface of the preform. In these unit-cells, there are two types of braided yarns in different directions and two bundles of quarter axial yarns, which are interlaced to form the surface layer of the preform. In addition, each unit-cell also contains two six-directional and seven-directional yarns, which are evenly distributed at the top and bottom of the unit-cell.

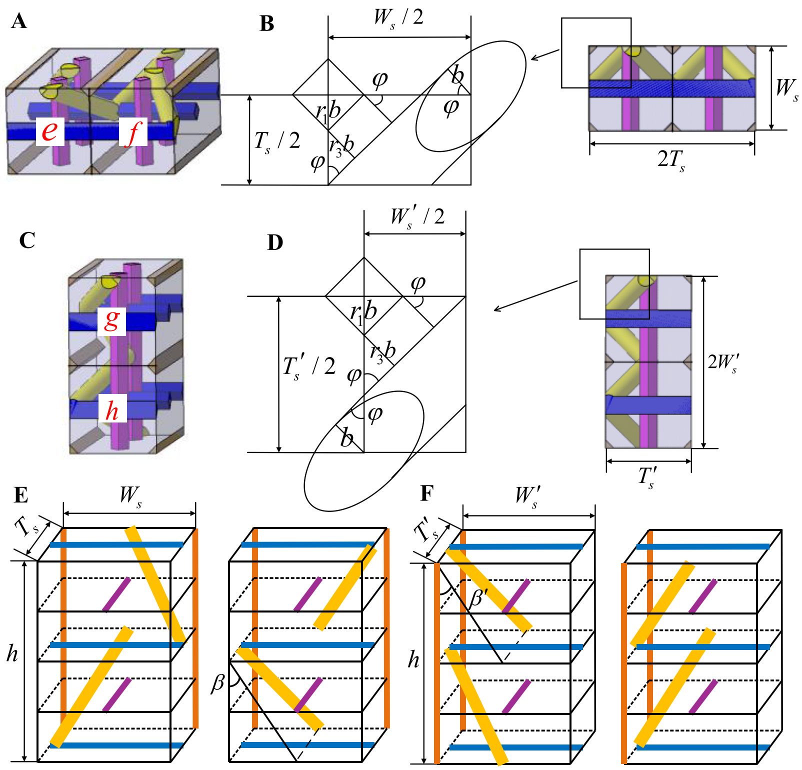

Figure 5: Surface unit-cell structure: 3D model (**A**,**C**), OXY projection (**B**,**D**) and yarn interweaving details (**E**,**F**).

According to the planar geometric relationships in Fig. 5B, the dimensions of the surface unit-cell along the width direction can be obtained as follows:

$$W_s = W_i = \frac{2\,(1 + r_3)\,b}{\cos\varphi} + 2r_1b \tag{13}$$

$$T_s = \frac{2r_3b}{\sin\varphi} + 2r_1b \tag{14}$$

$$\tan\beta = \frac{W_s}{h} = \frac{2\,(1 + r_3)\,b}{h\cos\varphi} + \frac{2r_1b}{h} \tag{15}$$

According to the planar geometric relationships in Fig. 5D, the dimensions of the surface unit-cell along the thickness direction can be obtained as follows:

$$W_s' = \frac{2r_3b}{\cos\varphi} + 2r_1b \tag{16}$$

$$T_s' = T_i = \frac{2b\,(1 + r_3)}{\sin\varphi} + 2r_1b \tag{17}$$

$$\tan\beta' = \frac{W_s'}{h} = \frac{2r_3b}{h\cos\varphi} + \frac{2r_1b}{h} \tag{18}$$

2.6 Parametric Calculation of the Corner Unit-Cell

The corner unit-cell structure of the preform as shown in Fig. 6A. Fig. 6C shows the yarn interlacing structure of the unit-cell in the corner area of the 3D seven-directional braided preform, and this structure corresponds to the area *i* in Fig. 2B. The arrangement direction of the corner unit-cell is parallel to the surface of the preform. In the corner unit-cell, there is only one orientation of braided yarns. Compared with the unit-cell structures in other areas, it shows different yarn distribution characteristics. In addition to the braided yarns, the corner unit-cell also contains one quarter of an axial yarn, as well as two six-directional and seven-directional yarns, which are evenly distributed on the top and bottom surfaces of the unit-cell.

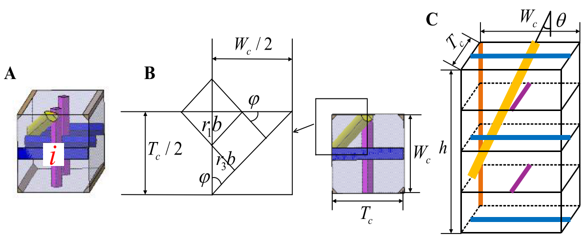

Figure 6: Corner unit-cell structure: 3D model (**A**), OXY projection (**B**) and yarn interweaving details (**C**).

According to the planar geometric relationships in Fig. 6B, the dimensions of the corner unit-cell along the thickness direction can be obtained as follows:

The corner unit-cell width W_c equals the surface unit-cell width in the thickness direction ($W_c = W_s'$), and the corner unit-cell thickness T_c equals the surface unit-cell thickness in the width direction ($T_c = T_s$). These relationships follow the geometric framework established by Li et al. [16].

$$W_c = W_s' = \frac{2r_3 b}{\cos\varphi} + 2r_1 b \tag{19}$$

$$T_c = T_s = \frac{2r_3 b}{\sin\varphi} + 2r_1 b \tag{20}$$

$$\tan\theta = \frac{8b}{3h\sin 2\varphi}\sqrt{r_3^2 + 2r_1 r_3 \sin^2\varphi\cos\varphi + 2r_1 r_3 \sin\varphi\cos^2\varphi + 2r_1^2\sin^2\varphi\cos^2\varphi} \tag{21}$$

2.7 Fiber Volume Fraction and Unit-Cell Mass

The fiber volume fraction is a key indicator for evaluating the performance of fiber-reinforced composites. By establishing a parametric model of the unit-cell structure of 3D seven-directional braided composites and combining the yarn parameters with the unit-cell geometric parameters, the fiber volume fraction of the material can be calculated. More detailed procedures can be found in the Supporting Information.

Finally, the fiber volume fraction of the unit-cell is:

$$V_{ff} = \varepsilon \times V_f \tag{22}$$

The mass calculation formula of the unit-cell of the 3D seven-directional braided material is as follows:

Regarding the validation comparison (as shown in Table 1), the finite element simulations in this study were performed at $V_f = 40\%$, which is a reasonable value for the parametric geometric model that avoids yarn entanglement while capturing the parametric trends. For direct comparison with the experimental data at $V_f \approx 52\%$ [52], the elastic constants were calculated using the theoretical bridging model at the corresponding fiber volume fraction. The theoretical predictions at V_f = 52% are consistent with the FE trends at V_f = 40%, supporting the validity of this approach for cross-volume-fraction comparison.

Table 1: Comparison between simulation and experimental results of 3D seven-directional braided composites.

Sample	γ (°)	V_f (%)	Axial Elastic Modulus (GPa)		
			Experiment	Prediction	Error
3D7d-1	20	51.2	74.9	71.6	4.4%
3D7d-2	40	52.2	42.2	41.2	2.4%

The parameter V_{ff} is defined as the product $V_{ff} = V_f \times \varepsilon$, where V_f is the overall fiber volume fraction of the composite and ε is the fiber packing factor (the ratio of total fiber cross-sectional area to yarn cross-sectional area within a single yarn bundle). Physically, V_f represents the volume of fibers relative to the total composite volume, while ε accounts for the fact that yarns are not 100% fiber—they contain matrix-rich regions between individual filaments. Thus, $V_{ff} = V_f/\varepsilon$ would represent the effective yarn volume fraction, and the product $V_f \times \varepsilon$ provides a combined metric that simultaneously captures both the macroscopic fiber loading and the microscopic packing efficiency of the yarn bundles. This dual dependence is critical for accurately translating braiding parameters into predicted elastic properties.

$$Y_f = C_i Y_i + C_s Y_s + C_s' Y_s' + C_c Y_c \tag{23}$$

$$U = C_i U_i + C_s U_s + C_s' U_s' + C_c U_c \tag{24}$$

$$m = Y_f \rho_f + \left(U - Y_f\right) \rho_m \tag{25}$$

2.8 Parametric Design and Implementation of a Meso-Structure Modeling System for 3D Seven-Directional Braided Composite

For the parametric model of the 3D seven-directional braided composite material established in this paper, a supporting automated modeling tool has been developed. The source code of the tool can be found in the folder "BraidedCompositesGenerate". Readers can run the plugin by copying this folder to the "Abaqus_plugins" folder in the working directory of Abaqus (the tested and approved version is Abaqus 2022, and the operating system is Windows).

In the RSG Dialog Builder, controls such as Group Box, Text Box, Button, and Icon are used to build the interactive interface of the composite material parametric design system, which includes a parameter input area, a model preview area, and an operation button area. Through this interface, by inputting the braiding parameters, the parameter calculation of the internal cell model can be completed, and the solid model of the internal cell can be generated. Its graphical interface is shown in Fig. S1.

After completing the parameter input, the component assembly stage begins. First, all the braiding yarns are numbered, as shown in Fig. S2A. The numberings of the axial yarn, six-directional yarn, and seven-directional yarn are shown in Fig. S2B. In the Abaqus assembly module, the braiding yarns are instantiated as 10 independent yarns, and their spatial poses are adjusted through rotation vectors and translation operations. The specific operations are detailed in Table S1 for yarn numbers 1–10. The axial yarn, six-directional yarn, and seven-directional yarn are instantiated separately, and then the overall layout is completed through rotation vectors and array operations. The specific operations are shown in Table S1 for yarn numbers 11–13.

2.9 Mechanical Property Finite Element Analysis Method

When solving for the mechanical properties of 3D seven-directional braided composites, first, based on the elastic properties of T300 carbon fibers and TDE-86 matrix in Table 2, the equivalent elastic properties of fiber bundles are obtained through the bridging model [53] (as shown in Table 2). The RVE-based finite element modeling approach using DIGIMAT and ABAQUS has been widely adopted for composite microstructure analysis.

Table 2: Elastic properties of fibers and resin matrix.

	E_{11} (GPa)	E_{22} (GPa)	G_{12} (GPa)	G_{23} (GPa)	μ_{12}	μ_{23}
T300 carbon fiber	220	13.8	9.0	4.8	0.2	0.25
TDE-86	3.45	3.45	1.28	1.28	0.35	0.35
Fiber bundle	198.35	11.86	6.62	4.07	0.22	0.30

The mechanical properties of 3D seven-directional braided composites were analyzed using the finite element method, with the specific analysis process shown in Fig. 7. First, unit-cell models with different braiding angles were rapidly established through Abaqus secondary development tools. Subsequently, periodic meshing of the models was performed in Hypermesh, and mapped meshing was used to ensure one-to-one matching of nodes on the opposite faces of the unit-cell. After importing the mesh model into Abaqus, sets were created for the seven types of fiber bundles (4 types of braiding yarns, 1 type of axial yarns, 1 type of six-directional yarns, and 1 type of seven-directional yarns), respectively, and local coordinate systems were set (Fig. 8A–G), with corresponding material properties assigned simultaneously. Six reference points (RP) were introduced to apply periodic boundary conditions, and a Python program was used to establish constraint equations for nodes on the opposite faces of the unit-cell to ensure deformation consistency (Fig. 8H). Displacement loads (tensile and shear) were applied through the RP points, and reaction forces were extracted. After solving, stress and strain contour plots under different loads were obtained (Supporting Material Fig. S3), and engineering constants were calculated through post-processing: Young's modulus was derived from the ratio of stress to strain (Eq. (26)), Poisson's ratio was the ratio of transverse strain to axial strain (Eq. (27)), and shear modulus was calculated from the ratio of shear stress to shear strain (Eq. (28)). Finally, elastic property parameters under braiding angles ranging from 20° to 70° were obtained (Table 3). Numerical simulation of structural components using finite element methods has been demonstrated in various engineering applications.

$$E = \frac{\text{stress}}{\text{axial strain}} = \frac{\frac{\Sigma\text{surface node force}}{\text{surface area}}}{\frac{\Delta L}{L}} \tag{26}$$

$$\nu = \frac{\text{transverse strain}}{\text{axial strain}} = \frac{\frac{\Delta H}{L}}{\frac{\Delta L}{L}} \tag{27}$$

$$G = \frac{\text{shear stress}}{\text{shear strain tensor}} = \frac{\frac{\Sigma\text{surface node force}}{\text{surface area}}}{\frac{\Delta 1}{L} + \frac{\Delta 2}{L}} \tag{28}$$

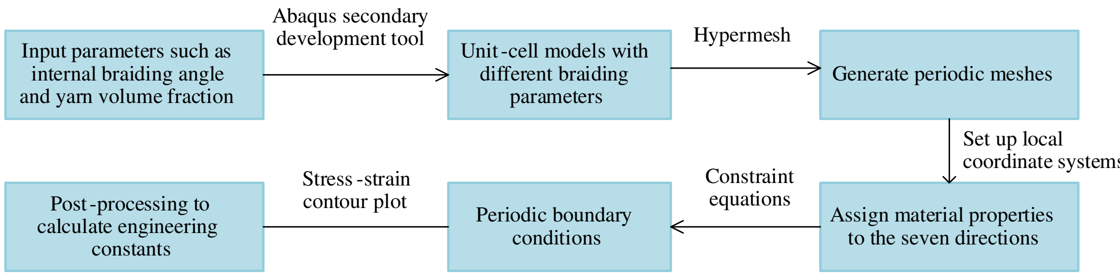

Figure 7: Finite element analysis process.

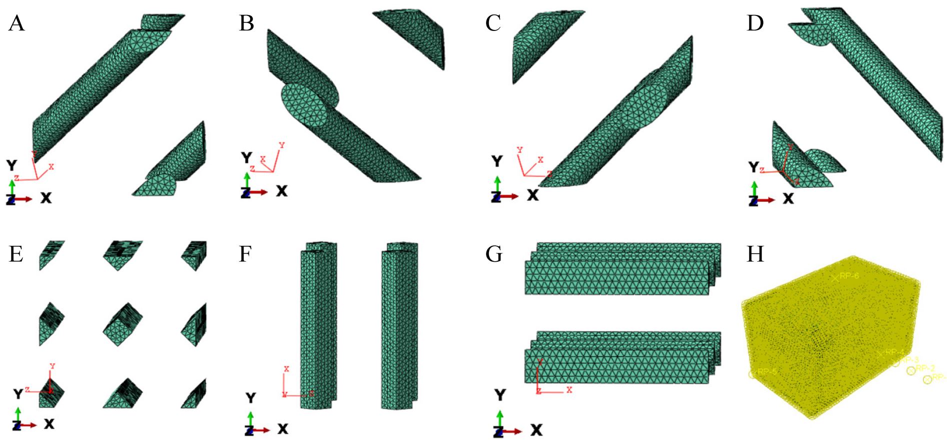

Figure 8: (**A–G**) Local coordinate systems of fiber bundles: (**A–D**) braiding yarns, (**E**) axial yarn, (**F**) six-directional yarn, (**G**) seven-directional yarn; (**H**) application of periodic boundary conditions.

Table 3: Predicted elastic properties of 3D seven-directional braided composites (V_f = 40%).

	E_{11} (GPa)	E_{22} (GPa)	G_{12} (GPa)	G_{23} (GPa)	μ_{12}	μ_{23}
20°	46.61	19.90	4.13	2.15	0.21	0.15
30°	37.55	19.87	5.59	2.63	0.26	0.14
40°	29.00	20.12	6.53	3.64	0.28	0.15
50°	23.16	20.93	6.49	5.21	0.25	0.19
60°	20.46	22.30	5.51	7.19	0.19	0.26
70°	19.80	23.71	3.97	9.10	0.13	0.33

2.10 Finite Element Formulation and Mesh Convergence

The finite element analysis is based on the standard linear elasticity theory. The unit-cell domain with periodic boundary conditions is governed by the equilibrium equations, constitutive relations, and kinematic equations, which together form the boundary value problem. Using the principle of virtual work, the problem is transformed into its weak form and discretized with 4-node tetrahedral elements (C3D4 in Abaqus), resulting in the linear system $Ku = f$. The effective elastic constants (E_{11}, E_{22}, G_{12}, ν_{12}, etc.) are then extracted from volume-averaged stress and strain responses under six independent loading cases following standard homogenization procedures. The elasticity tensor C is constructed from the equivalent yarn properties obtained via the bridging model (Table 2), which depends on V_f, braiding angle γ, and the T300/TDE-86 material properties.

Mesh convergence was verified by refining the discretization across four levels with approximately 50,000, 100,000, 200,000, and 400,000 elements. The relative error in predicted longitudinal modulus E_{11} between the two finest meshes was less than 0.5%. Representative load-deflection curves for each refinement level are provided in the Supplementary Material, confirming the absence of mesh bias.

Rigorous finite element discretization of coupled mechanical problems, as demonstrated by Ortiz-Toranzo and Romero [54] for thermo-diffusive-mechanical systems with large deformations, underscores the importance of consistent variational formulations for ensuring solution accuracy and convergence.

3 Results

3.1 Development of 3D Seven-Directional Braided Composites

This study successfully addressed the key technical challenges in multi-scale modeling of 3D seven-directional braided composites through an integrated approach combining theoretical modeling, parametric analysis, and tool development. Fig. 2 presents the integrated workflow for parametric modeling and design of 3D seven-directional braided composites, comprising five key components: (A) the four-step braiding process demonstrating yarn carrier movements and interlacing patterns in the preform; (B) yarn movement paths in the horizontal plane, showing braided yarns' parallel oblique trajectories with alternating interior-surface movement, two opposing parallel path sets of adjacent yarns, and horizontal/vertical paths for six-directional/seven-directional yarns; (C) construction of representative unit-cell models (internal, surface, and corner types) with associated parametric symbols for structural characterization; (D) systematic derivation of mathematical relationships between key geometric and mechanical parameters; and (E) the architecture of the parametric design system, featuring interactive GUI interfaces for input control and kernel modules for automated model generation and parameter calculation. This workflow establishes a complete digital thread from braiding processes to structural performance, enabling efficient design optimization of 3D seven-directional braided composites while providing standardized inputs for subsequent performance predictions.

3.2 Rules and Assumptions of Seven-Directional Rectangular Braiding

The 3D seven-directional braided composite is fabricated using two distinct yarn groups: the first group comprises braiding yarns and axial yarns, while the second group consists of perpendicular six-directional and seven-directional yarns. During the braiding process, yarn carriers follow a specific movement sequence to form the cross-sectional profile characteristic of 3D seven-directional preforms. This manufacturing process employs a four-step rectangular braiding technique. (Detailed methodology is provided in the Methods Section 2.2).

In the braided preform, the yarns exist in bundles, and these bundles are independent of each other. Their cross-sections are mainly elliptical. Due to the extrusion of the yarns, the cross-sections of the axial yarns, six-directional yarns, and seven-directional yarns are mainly rhombic. Therefore, before conducting a meso-scale analysis of 3D seven-directional braided composites, the following assumptions are made:

(1) The cross-section of the braided yarns in the preform is elliptical, with the major semi-axis length of a and the minor semi-axis length of b.
(2) The cross-section of the axial yarns in the preform is square, with the side length of $\sqrt{2}r_1 b$.
(3) The cross-sections of the six-directional and seven-directional yarns are rhombic, with the diagonal lengths of $2r_2 b$ and $2r_2 b/\tan\alpha$.
(4) The braiding process within a certain braiding length is relatively stable to ensure the uniformity of the braided structure.

(5) All the yarns in the pre-form are of the same material, with the same fineness and flexibility.
(6) The braided yarns have the same fiber packing factor ε.

The constraints of geometric trajectories ensure the orderliness of yarn intersections: Braiding yarns follow parallel oblique trajectories, with adjacent yarns forming reverse parallel paths (Fig. 2B), and avoid transverse entanglement through alternating "interior-surface" movements; Six-directional/seven-directional yarns are distributed along horizontal/vertical paths, respectively (Fig. 2B), orthogonal to the trajectories of braiding yarns and located in different planes, thus reducing interlayer cross-interference. On the other hand, the cross-sectional dimensions of yarns (semi-major axis a and semi-minor axis b of the ellipse, side length of the square $\sqrt{2}r_1b$, and diagonals $2r_2b$ and $2r_2b/\tan\alpha$ of the rhombus) are correlated through geometric relationships, ensuring that yarns maintain gap matching after extrusion at intersections and avoiding excessive overlap.

It should be noted that the internal braiding angle γ used throughout parametric analysis is a geometric parameter derived from the yarn trajectory within the unit-cell and is distinct from the surface braid angle α_s that is visually measurable on the exterior of the preform. The mechanical braiding angle γ_m, which represents the actual inclination of yarns under process-induced tension and compaction, may differ from both γ and α_s due to yarn straightening and nesting effects. The relationship $\gamma_m = f(\gamma, \alpha_s, \text{compaction})$ requires experimental calibration for each material system and braiding machine configuration. In the present study, all analyses use the internal braiding angle γ as defined by the geometric model, and the reader should be aware of this distinction when interpreting results in the context of braiding machine setup parameters.

3.3 Analysis of the Three-Unit-Cell Structure of 3D Seven-Directional Braided Composites

Based on the cross-sectional shapes of the three yarn types in 3D seven-directional braiding, their respective cross-sectional areas can be calculated: S_1 (elliptical cross-sectional area of braiding yarns), S_2 (square cross-sectional area of axial yarns), and S_3 (rhombic cross-sectional area of six-directional and seven-directional yarns). The braiding angles (α, β, β', θ) are derived from the yarn trajectories, which are determined by the step length and frequency of the carrier movements. These angles are indirectly calculated through geometric relationships as a result of the combined motion in the X and Y directions. According to the assumptions, different types of yarn bundles must possess identical fiber packing factors (ε).

Fig. 9 illustrates the division of unit-cell regions (internal, surface, and corner) in the 3D braided composite. Subsequently, based on the specific yarn interlacing patterns and geometric relationships, the following parameters can be calculated: internal unit-cell parameters (W_i, T_i, α), surface unit-cell parameters (W_s, T_s, β, W_s', T_s', β'), corner unit-cell parameters (W_c, T_c, θ), fiber volume fraction and unit-cell mass (V_{ff}, Y_f, U, m). The calculation formulas are presented in Table 4, with detailed computational procedures provided in the Methods Sections 2.4–2.7. A footnote indicates that definitions of all symbols in the formulas are given in Table S2 of the Supporting Information.

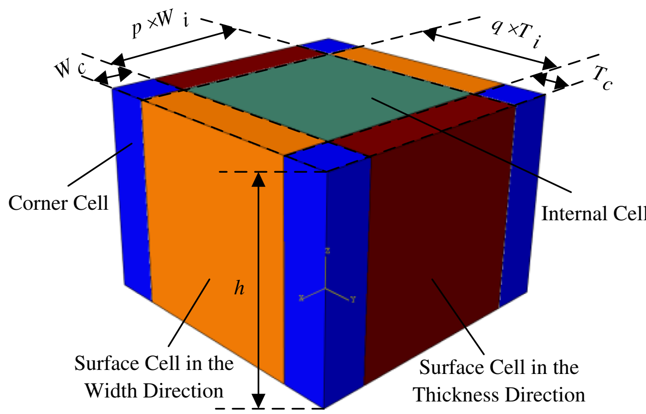

Figure 9: Division of three-unit-cell regions.

Table 4: Braiding parameters: symbol, definitions and calculations.

Symbol	Definition	Equation*
W_i	width of the internal unit-cell	Eq. (9)
T_i	thickness of the internal unit-cell	Eq. (10)
α	mechanical braiding angle	Eq. (11)
h	braiding pitch length	Eq. (12)
W_s	width of the surface unit-cell in the width direction	Eq. (13)
T_s	thickness of the surface unit-cell in the width direction	Eq. (14)
β	surface braiding angle in the width direction	Eq. (15)
$W_s^{'}$	width of the surface unit-cell in the thickness direction	Eq. (16)
$T_s^{'}$	thickness of the surface unit-cell in the thickness direction	Eq. (17)
β'	surface braiding angle in the thickness direction	Eq. (18)
W_c	width of the corner unit-cell	Eq. (19)
T_c	thickness of the corner unit-cell	Eq. (20)
θ	corner braiding angle	Eq. (21)
V_{ff}	fiber volume fraction of the unit-cell	Eq. (22)
Y_f	yarn volume of the unit-cell	Eq. (23)
U	volume of the unit-cell	Eq. (24)
m	mass of the unit-cell	Eq. (25)

Note: *See Table S2 in Supporting Information for additional symbol descriptions and equation references.

3.4 The Influence of the Variation of Cell Parameters of 3D Braided Composites

The 3D braided preform is usually made into the final size of the composite material. Subsequently, the braided preform can be cured with the matrix through various methods to form the composite material. This preform as a whole is composed of internal unit-cells, surface unit-cells and corner unit-cells. The size of the entire preform can be expressed as:

$$W = (q-1)\,W_i + 2W_c = \frac{2b\left[(q+1)\,(r_3 + r_1\cos\varphi) + q - 1\right]}{\cos\varphi} \tag{29}$$

$$T = (p-1)\,T_i + 2T_c = \frac{2b\left[(q+1)\,(r_3 + r_1\cos\varphi) + q - 1\right]}{\sin\varphi} \tag{30}$$

Among them, W is the width of the composite material, and T is the thickness of the composite material. The values of the braiding parameters in this subsection are shown in Table 5.

Table 5: Values of braiding parameters.

Parameter	Size
Horizontal orientation angle	$\varphi = 45°$
Semi-minor axis length of elliptical yarn	$b = 0.1$ mm
Cross-sectional dimension coefficient of axial yarn	$r_1 = 1$
Cross-sectional dimension coefficient of six-and seven-direction yarn	$r_2 = 1$
Density of carbon fiber	$\rho_f = 1.6$ g/cm^3
Density of matrix	$\rho_m = 1.15$ g/cm^3

Fig. 10A–C shows dimensional changes of unit-cells vs. geometric braiding parameter (r_3). In (A), internal and corner unit-cell width/thickness curves coincide completely, scaling proportionally with r_3 due to identical trigonometric relationships at 45° horizontal orientation φ. For surface unit-cells, (B) width-direction and (C) thickness-direction parameters exhibit symmetric linear growth with r_3, maintaining matched slope ratios (see Eqs. (13)–(17)). This symmetry arises from equivalent geometric constraints in orthogonal directions at 45° orientation.

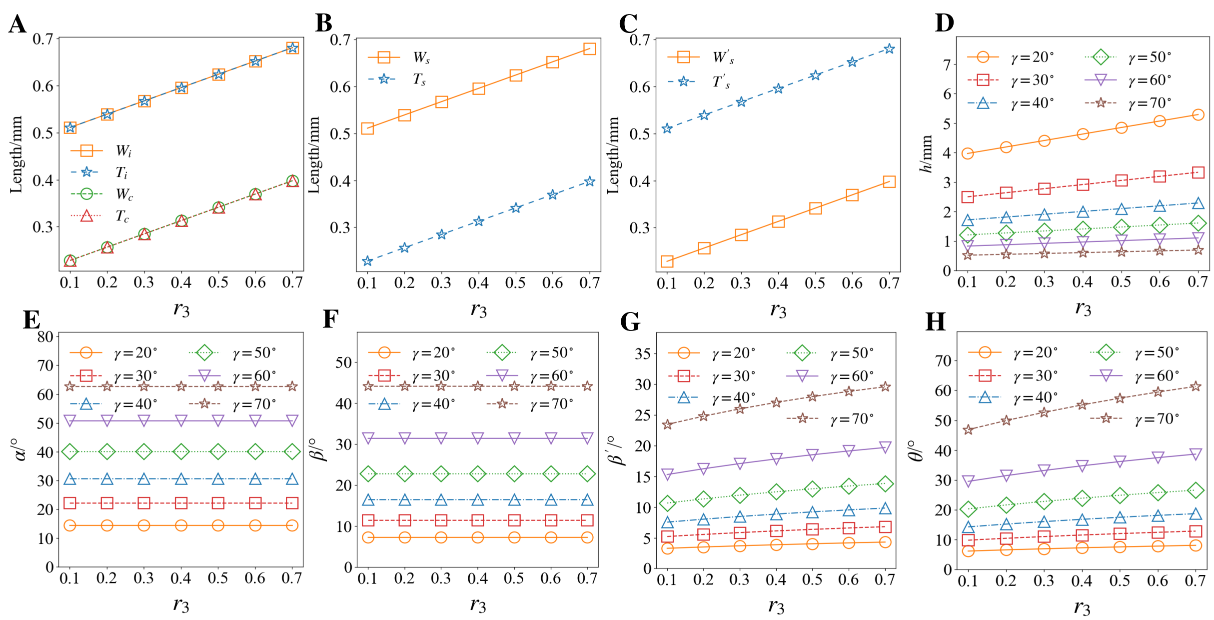

Figure 10: (Continued)

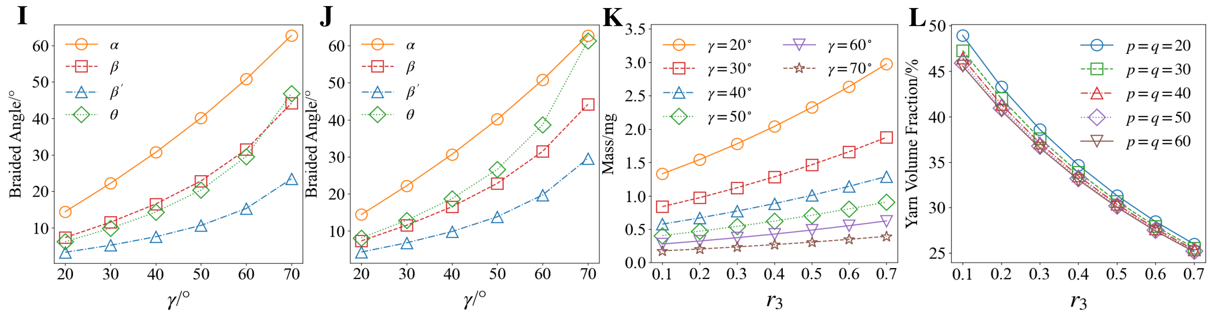

Figure 10: Multiscale geometric relationships in 3D braided composites: Unit-cell parameters evolution, braiding angle dependencies, fiber volume fraction, and mass correlations. (**A**–**C**) Dimension evolution of unit-cells with r_3: (**A**) internal & corner cell, (**B**) width-direction surface cell, and (**C**) thickness-direction surface cell; (**D**–**H**) Braiding parameter dependencies on r_3: (**D**) h, (**E**) α, (**F**) β, (**G**) β', and (**H**) θ; (**I**,**J**) Correlations between γ and characteristic angles (α, β, β', θ) at (**I**) $r_3 = 0.1$ and (**J**) $r_3 = 0.7$; (**K**,**L**) Effects of r_3 and yarn count on (**K**) m and (**L**) V_f.

Fig. 10D–H presents the parametric relationships in 3D braided composites. In (D), Braiding pitch length (h) scales linearly with braiding geometric parameter (r_3), showing greater sensitivity at smaller internal braiding angle (γ) due to unit-cell expansion; In (E) and (F), Mechanical (α) and width-direction surface angles (β) increase with γ but remain independent of r_3, governed solely by horizontal orientation φ and internal braiding angle γ (Eqs. (7)–(11)); In (G) and (H), Thickness-direction surface (β') and corner angles (θ) exhibit r_3-dependent growth that amplifies with increasing γ, resulting from enhanced yarn projection effects and pronounced geometric constraints at corners. The corner region demonstrates the most significant angular variations due to its heightened sensitivity to both r_3 and γ.

According to trigonometric functions, the relationships among the internal braiding angle, the mechanical braiding angle, the surface braiding angle, and the corner braiding angle are obtained:

$$\tan\gamma = \frac{1}{\sin\varphi}\tan\alpha = \frac{2}{\sin\varphi}\tan\beta = \frac{4\left(1+r_3\right)+4r_1\cos\varphi}{2r_3\sin\varphi+2r_1\sin\varphi\cos\varphi}\tan\beta' \tag{31}$$

$$\tan\gamma = \frac{\sqrt{r_3^2+2r_1r_3\sin^2\varphi\cos\varphi+2r_1r_3\sin\varphi\cos^2\varphi+2r_1^2\sin^2\varphi\cos^2\varphi}}{3\left(1+r_3+r_1\cos\varphi\right)}\tan\theta \tag{32}$$

Fig. 10I,J shows the relationships between four braiding angles (mechanical α, width-direction surface β, thickness-direction surface β', and corner θ angles) and the internal braiding angle (γ) under four braiding geometric parameter (r_3). The data in Fig. 10I,J correspond to cases where r_3 equals 0.1 and 0.7, respectively, while the remaining cases (r_3 = 0.3 and 0.5) are provided in the Fig. S4. All angles increase with γ, with more pronounced growth at higher γ values. Notably, β' and θ additionally exhibit r_3-dependence, showing amplified increases—especially for θ in corner regions due to enhanced geometric constraints.

Fig. 10K,L systematically analyzes the variations in fiber volume fraction (V_f) and unit-cell mass (m) of 3D braided composites under different braiding geometric parameter (r_3). In (K), m shows r_3-dependent growth, amplified at smaller internal braiding angle ($\gamma = 20°$) through enhanced fiber packing; In (L), V_f converges with yarn count (p, q) as internal unit-cells dominate at $p, q > 50$. (Complementary analyses of r_3-induced unit-cell expansion effects on V_f reduction and the linear mass–volume scaling relationship are detailed in Fig. S5 under fixed parameters $p = q = 40$ and $\theta = 45°$).

3.5 Performance of the Parametric Modeling System

Based on the above relationships of unit-cell parameters, this study has developed an Abaqus-Python parametric modeling plugin (for details, see the Supporting Material "BraidedCompositesGenerate"); the plugin development process is shown in Fig. 11. Our preceding analysis of three-unit-cell structures in 3D seven-directional braided materials has confirmed that the internal unit-cell plays a dominant role in determining the composite's macroscopic mechanical properties. Therefore, the plugin specifically focuses on rapid modeling and parametric design of internal unit-cells, which can quickly generate representative volume element models under different braiding parameters. By inputting parameters such as the braiding angle, yarn dimensions, and yarn volume fraction, this tool automatically calculates the geometric dimensions and constructs a unit-cell entity that includes braiding yarns, six-directional yarns, seven-directional yarns, and the matrix. Among them, it solves the problems of low efficiency and high error-proneness in manual modeling, and provides a standardized input for subsequent mechanical property analysis.

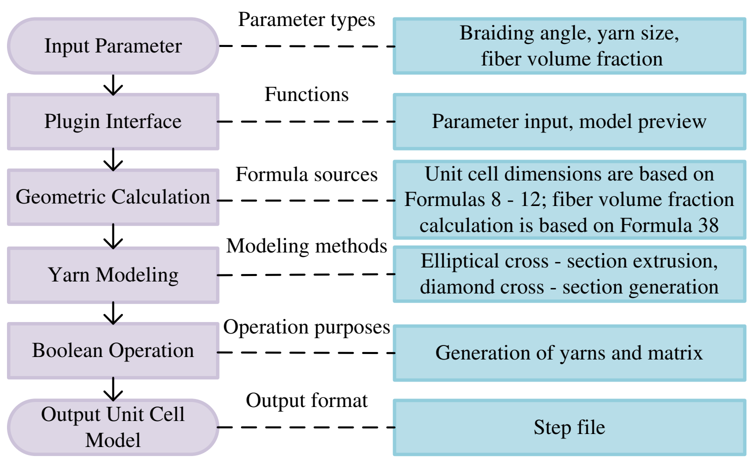

Figure 11: Workflow of the Abaqus-Python parametric modeling plugin for automated unit-cell generation.

Utilizing the aforementioned parametric design system, we successfully constructed multiple sets of unit-cell models with typical braiding parameters (Fig. S6). A systematic comparison was then performed between theoretical values and plugin output values for key model parameters (braiding pitch length h, fiber volume fraction V_f, and unit-cell mass m), as documented in Table S3.

As quantitatively demonstrated in Fig. 12, the error rates of these parameters exhibit distinct r_3-dependence: For five discrete r_3 values ($\gamma = 20°$), the error distributions of h, V_f, and m are presented as clustered columns. The results confirm that all error rates between plugin outputs and theoretical values remain below 1% (Table S3), which effectively validates both the high precision and reliability of this tool in geometric modeling and parameter calculation. This verification establishes an accurate foundation for subsequent mechanical property analysis. [Note: this represents software self-consistency verification, not physical validation].

It is important to clarify that the error rates reported above (all below 1%) represent a self-consistency verification between the plugin-generated geometry and the analytical equations. This verification confirms that the software correctly implements the idealized geometric formulas described in Sections 2.4–2.6, but does not constitute a physical validation of the geometric model against experimental measurements of real composite microstructures. Physical validation would require comparison of the model-predicted yarn geometries and volume fractions with micro-CT or optical microscopy data from manufactured specimens.

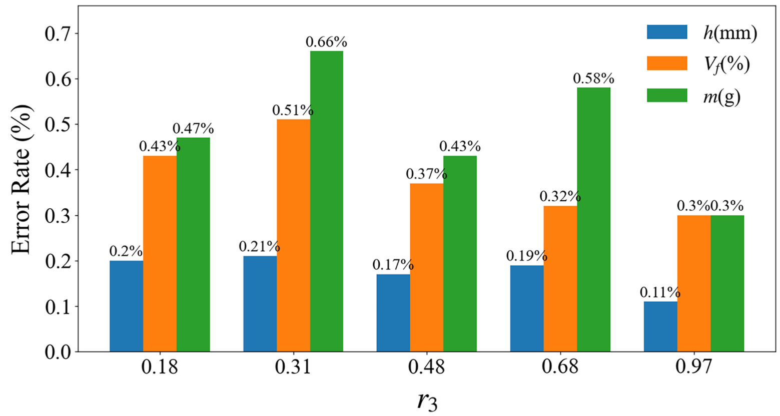

Figure 12: Error rates for different parameters by r_3 values.

3.6 Mechanical Property Analysis and Verification

Through the finite element analysis [55,56] of the 3D seven-directional unit-cell model (see Section 2.9 for details), the mechanical property parameters of the 3D seven-directional braided composites are obtained, and their advantages and reliability are verified by comparison. The elastic properties of the unit-cell in various directions under different braiding angles obtained through the analysis are shown in Table 3.

To verify the mechanical property advantages of the 3D seven-directional braided structure, the predicted elastic modulus results of 3D four-directional and five-directional braided composites from published literature [57–60] were selected and compared with the longitudinal and transverse elastic moduli of the seven-directional model in this paper (Fig. 13).

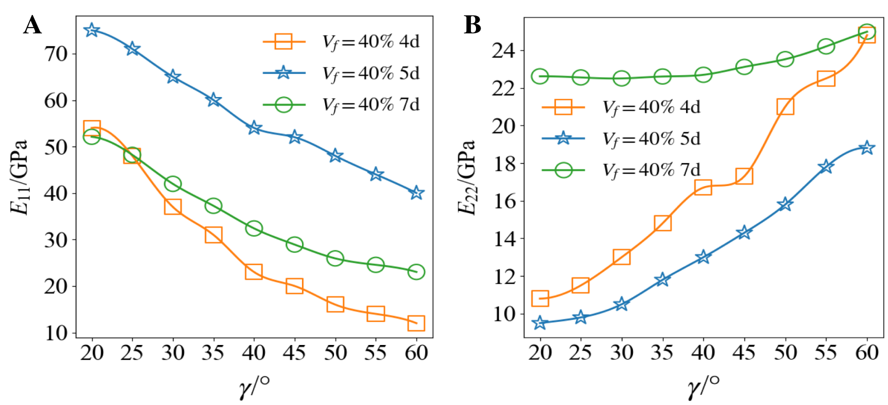

Figure 13: Variation of elastic modulus of composites with different braiding directions as a function of braiding angle. (**A**) Longitudinal elastic modulus (**B**) Transverse elastic modulus.

Combined with Fig. 13A,B, it can be seen that the performance differences between the seven-directional model and the four-directional and five-directional models vary regularly with the braiding angle, and the mechanism is closely related to yarn configuration and force transmission paths:

Compared with the four-directional model, the longitudinal modulus (E_{11}) of the seven-directional model is slightly lower than that of the four-directional model before 25°—this is because the yarns of the four-directional model have a higher proportion of longitudinal projection at small braiding angles, resulting in more concentrated longitudinal load-bearing. However, after 25°, the multi-directional yarns of the seven-directional model start to play a synergistic role; the six-directional/seven-directional yarns reduce longitudinal deformation through interlacing constraints, making E_{11} surpass and maintain the lead. In terms of transverse performance, due to the three-dimensional interlacing advantage of additional yarns, the seven-directional model is superior to the four-directional model throughout, with the advantage becoming more significant as the braiding angle decreases, reflecting the strengthening effect of multi-directional yarns on transverse force transmission paths.

Compared with the five-directional model, although the longitudinal modulus (E_{11}) of the seven-directional model is slightly lower overall (the five-directional structure has a higher proportion of axial yarns, leading to more prominent longitudinal load-bearing), its transverse modulus (E_{22}) is not only higher but also more stable with changes in braiding angle. This is attributed to the transverse "supporting framework" formed by the six-directional/seven-directional yarns in the seven-directional model, which maintains the uniformity of transverse stiffness even when the angle changes, effectively compensating for the weak transverse performance of traditional structures.

In summary, by optimizing yarn direction configuration, the seven-directional model gradually catches up with the four-directional model in longitudinal performance at small braiding angles and surpasses it comprehensively at large angles. Meanwhile, its transverse performance leads the four-directional and five-directional models throughout, showing the characteristics of "balanced improvement in longitudinal direction and continuous strengthening in transverse direction", making it more suitable for multi-axial complex stress scenarios.

To verify the reliability of the model, the published experimental data on the elastic modulus of 3D seven-directional braided composites [52] (the experimental material is T700-12K carbon fiber/TDE-86 matrix, with the braiding process consistent with that in this paper) were selected and compared with the simulation results of this paper. Table 1 shows that the errors between the simulated values of the axial elastic modulus E_{11} of the seven-directional model in this paper and the experimental data are all controlled within 5%. indicating that the model can accurately reflect the mechanical properties of the actual material. The errors mainly result from the ideal assumption of yarn cross-sections in the model (ignoring the yarn extrusion deformation in actual braiding) and the discreteness of experimental samples. The consistency between the simulation results and the experimental data verifies the effectiveness of the finite element model, providing reliable theoretical support for subsequent engineering applications.

Note on comparative analysis: The performance of the 3D seven-directional composite is compared against literature data for four- and five-directional composites that may differ in fiber volume fraction, constituent material properties, and fiber packing factors. These confounding factors should be considered when interpreting the apparent performance differences. A fully controlled experimental comparison using identical constituents and processing conditions across all architectures would be required for a definitive assessment.

4 Discussion

4.1 Interpretation of Parametric Analysis Results

The parametric analysis reveals that the 3D seven-directional braided composite offers a fundamentally different design space compared to conventional four- and five-directional architectures. The presence of the sixth and seventh-directional yarns introduces additional load paths in the transverse plane, which directly contributes to the enhanced transverse modulus E_{22} and shear modulus G_{12} observed in the finite element predictions. This mechanistic explanation is consistent with the geometric analysis: the six-directional yarns oriented along the width direction and the seven-directional yarns along the thickness direction act as transverse reinforcements, converting what would be matrix-dominated properties in four-directional composites into fiber-dominated properties. The trade-off is a modest reduction in longitudinal modulus E_{11}, as the volume fraction of axially aligned fibers decreases when transverse yarns are introduced.

The sensitivity of elastic properties to the braiding angle γ follows the expected trend for textile composites: increasing γ redirects fiber orientation away from the longitudinal axis, decreasing E_{11} while increasing E_{22}, G_{12}, and the Poisson ratios. However, the seven-directional architecture exhibits a notably flatter E_{22}-vs-γ curve compared to four-directional composites reported in the literature, indicating that the transverse reinforcement provided by the sixth and seventh yarns partially decouples the transverse stiffness from the braiding angle. This decoupling is practically significant because it allows designers to select braiding angles based on longitudinal stiffness requirements without severely compromising transverse performance—a degree of freedom not available in conventional architectures.

When interpreting the comparative results against four- and five-directional composites, it is important to note that the literature data used for comparison may involve different fiber volume fractions, constituent materials, and processing conditions. These confounding factors should be considered when assessing the apparent performance differences. The qualitative trends observed—particularly the enhanced transverse modulus and shear modulus in the seven-directional architecture—are presented with this caveat. A fully controlled experimental comparison using identical constituents and processing conditions across all architectures would be required for a definitive assessment.

The automated Abaqus-Python plugin developed in this work reduces the time required to generate a parametric unit-cell model from hours to minutes, enabling systematic parametric studies that would be impractical with manual modeling. The plugin's verification against analytical equations confirms its numerical correctness with errors below 1%, though this should be understood as a software validation step rather than a physical validation of the geometric assumptions. The modular architecture of the plugin allows extension to other braiding patterns (e.g., five-directional) and integration with optimization frameworks for inverse design of braiding parameters to meet target elastic properties.

From an application perspective, the demonstrated transverse property enhancement makes 3D seven-directional braided composites particularly attractive for structural components subjected to multiaxial loading, such as pressure vessels, rocket motor casings, and connecting rods. The parametric design framework provides a quantitative tool for tailoring the braiding parameters—braiding angle, yarn dimensions, and fiber volume fraction—to meet specific stiffness requirements along multiple axes. However, the practical deployment of this framework requires the experimental calibration of the relationship between machine-controllable parameters (carrier path, step length, pitch) and the internal geometric parameters (braiding angle, yarn cross-section) used in the model.

4.2 Limitations and Future Work

Despite the advances presented in this study, several limitations should be acknowledged. The geometric model relies on a set of idealized assumptions regarding yarn cross-sectional shapes. Specifically, braiding yarns are modeled as perfect ellipses, axial yarns as squares, and six/seven-directional yarns as rhombuses. In reality, yarn cross-sections are irregular due to mutual compaction during the braiding process, and no explicit geometric compatibility condition is enforced among adjacent yarns occupying the same spatial domain. This simplification may lead to non-physical fiber overlap or unattainable volume fractions in extreme parameter regimes.

Furthermore, the current modeling framework assumes a fixed horizontal orientation angle of 45°, a single yarn material system (T300 carbon fiber/TDE-86 epoxy), and a perfectly regular rectangular array of yarn carriers with uniform cross-sections. The generalization capability of the model to non-45° carrier paths, circular or tubular preform geometries, hybrid yarn types, and varying tow sizes has not been demonstrated and warrants future investigation. A collaborative research plan with Northwestern Polytechnical University has been initiated to extend the framework to alternative machine configurations, preform geometries, and yarn systems.

Regarding experimental validation, the comparison is currently limited to two axial modulus data points from a single published source [43]. Transverse modulus, shear modulus, Poisson's ratio, unit-cell dimensions, and fiber volume fraction have not been independently validated against experiments. The plugin-to-theory error rate of less than 1% reported in Section 3.5 is a self-consistency check confirming that the software correctly implements the idealized geometric equations; it does not constitute physical validation of the geometric model against real composite microstructures. A systematic experimental campaign has been planned in collaboration with Northwestern Polytechnical University to validate all predicted elastic constants against multi-angle, multi-parameter experimental data.

The comparative mechanical property analysis in Section 3.6 compares the seven-directional architecture against four- and five-directional literature data that may involve different fiber volume fractions, constituent materials, and fiber packing factors. The observed performance differences could therefore partially reflect these confounding variables rather than purely architectural advantages. Normalized comparisons accounting for V_f differences are recommended in future studies.

The current study does not include a quantitative uncertainty analysis. Key uncertain parameters such as yarn cross-sectional dimensions, braiding angle tolerances, and fiber volume fraction variability can significantly influence the predicted elastic properties. Future work should incorporate variance-based sensitivity analysis (e.g., Sobol' indices) to quantify the contribution of each uncertain input to the output variability. As an alternative modeling paradigm, the Deep Energy Method (DEM) proposed by Samaniego et al. [61] offers a variationally consistent, mesh-free approach that naturally accounts for uncertainties and can incorporate experimental data directly. While the present study adopts the parametric unit-cell finite element framework for its engineering practicality and integration with commercial software ecosystems, DEM represents a promising direction for future work on braided composite modeling.

Additionally, the internal braiding angle, identified as a key independent variable, is not directly controllable on a braiding machine. The relationship between the internal braiding angle, the surface braid angle (which is visually measurable), and the mechanical braiding angle experienced by the yarns requires further experimental calibration. Establishing this mapping would enhance the practical applicability of the parametric design framework for braiding machine operators.

5 Conclusions

This study established a novel model for 3D seven-directional braided composites. Through systematic parametric analysis, it explored the influence of key braiding parameters on geometric characteristics. Based on these parametric relationships, an efficient automated modeling method was successfully developed via Abaqus-Python secondary development. The developed modeling tool features high precision and significantly improves computational efficiency.

The current research not only provides a complete geometric modeling framework but also conducts finite element analysis using this model, with comparisons against experimental data, verifying the reliability of the model and the feasibility of the seven-directional structure. These achievements offer valuable theoretical guidance and technical support for the design and optimization of seven-directional braided composites.

Acknowledgement: Not applicable.

Funding Statement: This research was funded by the Key Research and Development Program of Shaanxi Province, China, grant number 2023GXLH-089 (awarded to Feizhou Li, FL), and the Science and Technology Plan Project of Yulin City, Shaanxi Province, grant number 2024-CXY-191 (awarded to Feizhou Li, FL).

Author Contributions: Xiyue Zhang: Writing—original draft, Methodology, Data curation, Conceptualization. Zhihai Hu: Writing—original draft, Methodology. Weiliang Zhang: Investigation, Programming guidance. Xindang He: Conceptualization. Gexia Yuan: Data curation. Yanwei Feng: Data curation. Yafeng Qi: Writing—review & editing. Feizhou Li: Writing—original draft, Methodology, Data curation, Conceptualization. All authors reviewed and approved the final version of the manuscript.

Availability of Data and Materials: Data will be made available on request.

Ethics Approval: Not applicable.

Conflicts of Interest: The authors declare no conflicts of interest.

Code and Data Availability: The Abaqus-Python parametric modeling plugin and associated input data developed in this study are available at the following GitHub repository: https://github.com/zxyzxx/BraidedCompositesGenerate.git. The repository includes the plugin source code, example input files, and documentation for reproducing the unit-cell models and finite element simulations presented in this work.

Supplementary Materials: The supplementary material is available online at https://www.techscience.com/doi/10.32604/cmc.2026.084077/s1. The following supplementary materials are uploaded separately with this submission: **Figure S1:** Graphical interface of the parametric design system for 3D seven-directional braided composite. **Figure S2:** Yarn numbering: (A) Braiding yarns; (B) Axial yarns, six-directional yarns and seven-directional yarns. **Figure S3:** Results of unit-cell mechanical response: (a)~(c) Tension in X, Y, Z directions; (d)~(f) Shear in XY, XZ, YZ directions. **Figure S4:** Correlation between γ and four characteristic angles (α, β, β', θ) at different r_3: (A) $r_3 = 0.3$, (B) $r_3 = 0.5$. **Figure S5:** Effects of r_3 and yarn count on V_f (A) and m (B). **Figure S6:** Solid models of the internal unit-cells with typical braiding parameters: (A) $\gamma = 45°$, $V_f = 40\%$, (B) $\gamma = 45°$, $V_f = 30\%$, (C) $\gamma = 30°$, $V_f = 40\%$. **Table S1:** Rotation parameters of yarn instances. **Table S2:** Braiding parameters: symbol and definitions. **Table S3:** Comparison table between theoretical values and output parameters of the plugin.

References

1. Sun X, Sun C. Mechanical properties of three-dimensional braided composites. Compos Struct. 2004;65(3–4):485–92. doi:10.1016/j.compstruct.2003.12.009.
2. Bilisik K. Three-dimensional braiding for composites: a review. Text Res J. 2013;83(13):1414–36. doi:10.1177/0040517512450766.
3. Shi B, Liu S, Siddique A, Zhang J, Gu B, Sun B. Comparisons on impact fracture behavior between three-dimensional four directional and five directional braided composite materials. Int J Damage Mech. 2019;28(7):990–1020. doi:10.1177/1056789518805218.
4. Sun HY, Qiao X. Prediction of the mechanical properties of three-dimensionally braided composites. Compos Sci Technol. 1997;57(6):623–9. doi:10.1016/S0266-3538(96)00154-6.
5. Fujihara K, Yoshida E, Nakai A, Ramakrishna S, Hamada H. Influence of micro-structures on bending properties of braided laminated composites. Compos Sci Technol. 2007;67(10):2191–8. doi:10.1016/j.compscitech.2005.08.003.
6. Singh DB, Singh BN. New higher order shear deformation theories for free vibration and buckling analysis of laminated and braided composite plates. Int J Mech Sci. 2017;131(2):265–77. doi:10.1016/j.ijmecsci.2017.06.053.

7. Zeng T, Wu LZ, Guo LC. Mechanical analysis of 3D braided composites: a finite element model. Compos Struct. 2004;64(3–4):399–404. doi:10.1016/j.compstruct.2003.09.041.
8. Miravete A, Bielsa JM, Chiminelli A, Cuartero J, Serrano S, Tolosana N, et al. 3D mesomechanical analysis of three-axial braided composite materials. Compos Sci Technol. 2006;66(15):2954–64. doi:10.1016/j.compscitech.2006.02.015.
9. Xu K, Chen W, Liu L, Zhao Z, Luo G. A hierarchical multiscale strategy for analyzing the impact response of 3D braided composites. Int J Mech Sci. 2021;193(12):106167. doi:10.1016/j.ijmecsci.2020.106167.
10. Zhang W, Li C, Li L, Wang W, Yang L, Zhang C, et al. Numerical analysis on mechanical properties of 3D five-directional circular braided composites. Processes. 2025;13(3):800. doi:10.3390/pr13030800.
11. Gu Q, Quan Z, Yu J, Yan J, Sun B, Xu G. Structural modeling and mechanical characterizing of three-dimensional four-step braided composites: a review. Compos Struct. 2019;207:119–28. doi:10.1016/j.compstruct.2018.09.065.
12. He C, Ge J, Zhang B, Gao J, Zhong S, Liu WK, et al. A hierarchical multiscale model for the elastic-plastic damage behavior of 3D braided composites at high temperature. Compos Sci Technol. 2020;196(12):108230. doi:10.1016/j.compscitech.2020.108230.
13. Li DS, Lu ZX, Chen L, Li JL. Microstructure and mechanical properties of three-dimensional five-directional braided composites. Int J Solids Struct. 2009;46(18–19):3422–32. doi:10.1016/j.ijsolstr.2009.05.013.
14. Gao Y, Li J. Effects of braiding angle on modal experimental analysis of three-dimensional and five-directional braided composites. Compos Part B Eng. 2012;43(5):2423–8. doi:10.1016/j.compositesb.2011.11.025.
15. Du XB, Li DS, Jiang L, Fang DN. Numerical investigation on tensile behavior of three-dimensional six-directional braided composites. Int J Mech Sci. 2023;237(10):107815. doi:10.1016/j.ijmecsci.2022.107815.
16. Li DS, Fang DN, Jiang N, Yao X. Finite element modeling of mechanical properties of 3D five-directional rectangular braided composites. Compos Part B Eng. 2011;42(6):1373–85. doi:10.1016/j.compositesb.2011.05.042.
17. Du XB, Zhu H, Ai J, Li DS, Jiang L. Parameterized meso-scale modeling and experimental study on the tensile damage evolution and strength of 3D five-directional braided composites. Mater Des. 2021;205(8):109702. doi:10.1016/j.matdes.2021.109702.
18. Cui C. Full-size computer simulation model design of 3D braided composites. Mari Papel Y Corrugado. 2024;2024:98–105.
19. Ko FK, Pastore CM. Structure and properties of an integrated 3-D fabric for structural composites. Conshohocken, PA, USA: West; 1985. p. 428–39.
20. Li W, Hammad M, El-Shiekh A. Structural analysis of 3-D braided preforms for composites part I: the four-step preforms. J Text Inst. 1990;81(4):491–514. doi:10.1080/00405009008658725.
21. Yang JM, Ma CL, Chou TW. Fiber inclination model of three-dimensional textile structural composites. J Compos Mater. 1986;20(5):472–84. doi:10.1177/002199838602000505.
22. Kalidindi SR, Franco E. Numerical evaluation of isostrain and weighted-average models for elastic moduli of three-dimensional composites. Compos Sci Technol. 1997;57(3):293–305. doi:10.1016/S0266-3538(96)00119-4.
23. Wu DL. Three-cell model and 5D braided structural composites. Compos Sci Technol. 1996;56(3):225–33. doi:10.1016/0266-3538(95)00136-0.
24. Zeng T, Wu L. Post-buckling analysis of stiffened braided cylindrical shells under combined external pressure and axial compression. Compos Struct. 2003;60(4):455–66. doi:10.1016/S0263-8223(03)00018-7.
25. Pandey R, Hahn HT. Visualization of representative volume elements for three-dimensional four-step braided composites. Compos Sci Technol. 1996;56(2):161–70. doi:10.1016/0266-3538(95)00137-9.
26. Xu K, Xu XW. Finite element analysis of mechanical properties of 3D five-directional braided composites. Mater Sci Eng A. 2008;487(1–2):499–509. doi:10.1016/j.msea.2007.10.030.
27. Chen L, Tao XM, Choy CL. Mechanical analysis of 3-D braided composites by the finite multiphase element method. Compos Sci Technol. 1999;59(16):2383–91. doi:10.1016/S0266-3538(99)00087-1.
28. Zhai J, Zeng T, Xu GD, Wang ZH, Cheng S, Fang DN. A multi-scale finite element method for failure analysis of three-dimensional braided composite structures. Compos Part B Eng. 2017;110(23):476–86. doi:10.1016/j.compositesb.2016.11.039.

29. Wang B, Zhang G, Nie X, Wu C. A multi-scale finite element approach for the mechanical behavior analysis of 3D braided composite structures. Compos Struct. 2022;279:114711. doi:10.1016/j.compstruct.2021.114711.
30. Tang ZX, Postle R. Mechanics of three-dimensional braided structures for composite materials-part I: fabric structure and fibre volume fraction. Compos Struct. 2000;49(4):451–9. doi:10.1016/S0263-8223(00)00082-9.
31. Ma W, Zhu J, Jiang Y. Studies of fiber volume fraction and geometry of variable cross-section tubular 3D five-direction braided fabric. J Compos Mater. 2012;46(14):1697–704. doi:10.1177/0021998311422953.
32. Lu Z, Yang Z, Li Z. Development of investigation into mechanical behaviour of three dimensional braided composites. Acta Mater Compos Sin. 2004;21(2):1–7.
33. Zhu H, Du XB, Li DS, Jiang L. Investigation of parameterized braiding parameters and loading directions on compressive behavior and failure mechanism of 3D four-directional braided composites. Compos Struct. 2022;287(4):115357. doi:10.1016/j.compstruct.2022.115357.
34. Zhang D, Zheng X, Zhou J, Song X, Jia P, Liu H, et al. Effect of braiding architectures on the mechanical and failure behavior of 3D braided composites: experimental investigation. Polymers. 2022;14(9):1916. doi:10.3390/polym14091916.
35. Li DS, Yang X, Zhu H, Jiang L, Fang DN. Unit-cell geometry and mechanical properties of three-dimensional seven-directional braided composites. Thin Walled Struct. 2023;182(3):110299. doi:10.1016/j.tws.2022.110299.
36. Zhang C, Li N, Wang W, Binienda WK, Fang H. Progressive damage simulation of triaxially braided composite using a 3D meso-scale finite element model. Compos Struct. 2015;125(3):104–16. doi:10.1016/j.compstruct.2015.01.034.
37. He C, Ge J, Qi D, Gao J, Chen Y, Liang J, et al. A multiscale elasto-plastic damage model for the nonlinear behavior of 3D braided composites. Compos Sci Technol. 2019;171(12):21–33. doi:10.1016/j.compscitech.2018.12.003.
38. Ge L, Li H, Zhong J, Zhang C, Fang D. Micro-CT based trans-scale damage analysis of 3D braided composites with pore defects. Compos Sci Technol. 2021;211:108830. doi:10.1016/j.compscitech.2021.108830.
39. Liao X, Jiao Y, Xie J, Chen L. Fiber-level modeling of 3D braided preforms using virtual braiding method. Compos Struct. 2024;334(16):117988. doi:10.1016/j.compstruct.2024.117988.
40. Liu S, Wang A, Sun B, Liu S, Hu M, Jiang Q, et al. Investigation of the dynamic compression behavior of 3D braided composites based on a virtual fiber embedding method. Compos Struct. 2025;351(4):118592. doi:10.1016/j.compstruct.2024.118592.
41. Yang W, Jin Y, Yang Z, Zhang D. High-temperature tensile mechanical behavior and ablation mechanisms of three-dimensional multi-directions braided carbon/boron-modified phenolic composites. Polym Test. 2025;143(3):108703. doi:10.1016/j.polymertesting.2025.108703.
42. Li DS, Yang Y, Jiang L. Experimental study on the fabrication, high-temperature properties and failure analysis of 3D seven-directional braided composites under compression. Compos Struct. 2021;268(12):113934. doi:10.1016/j.compstruct.2021.113934.
43. Zhang F, Liu Z, Wu Z, Tao G. A new scheme and microstructural model for 3D full 5-directional braided composites. Chin J Aeronaut. 2010;23(1):61–7. doi:10.1016/S1000-9361(09)60188-6.
44. Wu L, Zhao F, Li Y, Sun X, Liu S, Jiang Q. Progressive damage analysis of three-dimensional hybrid braided composite under short beam shear loading. Compos Struct. 2023;313:116960. doi:10.1016/j.compstruct.2023.116960.
45. Zhang D, Zheng X, Wang Z, Wu T, Sohail A. Effects of braiding architectures on damage resistance and damage tolerance behaviors of 3D braided composites. Compos Struct. 2020;232(3–4):111565. doi:10.1016/j.compstruct.2019.111565.
46. Dang B, Tang J, Shang Y, Cai DA. Shear failure analysis of 3D seven-directional braided composites. Coatings. 2025;15(2):223. doi:10.3390/coatings15020223.
47. Zhang C, Xu X. Finite element analysis of 3D braided composites based on three unit-cells models. Compos Struct. 2013;98(5):130–42. doi:10.1016/j.compstruct.2012.11.003.
48. Zhang N, Kong X, Zhai J, Guo Z, Yan S, Duan Y, et al. Advances in multiscale modeling and mechanical properties characterization of 3D-braided composites. Adv Eng Mater. 2024;26(22):2401457. doi:10.1002/adem.202401457.
49. Zheng XT, Ye TQ. Microstructure analysis of 4-step three-dimensional braided composite. Chin J Aeronaut. 2003;16(3):142–50. doi:10.1016/S1000-9361(11)60175-1.

50. Han J, Wang R, Hu D, Bao J, Liu X, Guo X. A novel integrated model for 3D braided composites considering stochastic characteristics. Compos Struct. 2022;286(6):115309. doi:10.1016/j.compstruct.2022.115309.
51. Liu Y, Hou Y, Sapanathan T, Meng L, Xu Y. Multiscale modeling of the mechanical behavior of 3D braided CFRP composites under uniaxial tension. Compos Struct. 2023;306(12):116601. doi:10.1016/j.compstruct.2022.116601.
52. Luo G. Experimental comparative study on tensile and compressive properties of braided and laminated composites. J Civ Aviat Univ China. 2016;34(3):52.
53. Huang ZM. A bridging model prediction of the ultimate strength of composite laminates subjected to biaxial loads. Compos Sci Technol. 2004;64(3–4):395–448. doi:10.1016/S0266-3538(03)00220-3.
54. Ortiz-Toranzo A, Romero I. Finite element discretization of the thermo-diffusive-mechanical problem with large deformations. Rev Int Metodos Numer Calc Diseno Ing. 2024;40(4):64. doi:10.23967/j.rimni.2024.10.56364.
55. Wang Y, Liu ZG, Wei YC, Li ZJ, Yi YP, Wang YB. Novel processing technology and mesoscopic geometric modeling of a new three-dimensional (3D) braided composite and the study on its longitudinal mechanical properties. Compos Struct. 2020;251(13):112525. doi:10.1016/j.compstruct.2020.112525.
56. Zhou H, Hu D, Gu B, Sun B. Transverse impact performance and finite element analysis of three dimensional braided composite tubes with different braiding layers. Compos Struct. 2017;168:345–59. doi:10.1016/j.compstruct.2017.02.025.
57. Fang GD, Liang J, Wang Y, Wang BL. The effect of yarn distortion on the mechanical properties of 3D four-directional braided composites. Compos Part A Appl Sci Manuf. 2009;40(4):343–50. doi:10.1016/j.compositesa.2008.12.007.
58. Shokrieh MM, Mazloomi MS. A new analytical model for calculation of stiffness of three-dimensional four-directional braided composites. Compos Struct. 2012;94(3):1005–15. doi:10.1016/j.compstruct.2011.09.010.
59. Hu L, Liu Z, Wang Y, Ou J. Experiments and progressive damage analyses of three-dimensional full five-directional braided composites under three-point bending. Polym Compos. 2016;37(8):2478–93. doi:10.1002/pc.23435.
60. Zhang W, Wang X, Ji X, Tang X, Liu F, Liu S. Parametric characteristics analysis of three cells in 3D and five-directional annular braided composites. PLoS One. 2021;16(8):e0254691. doi:10.1371/journal.pone.0254691.
61. Samaniego E, Anitescu C, Goswami S, Nguyen-Thanh VM, Guo H, Hamdia K, et al. An energy approach to the solution of partial differential equations in computational mechanics via machine learning: concepts, implementation and applications. Comput Meth Appl Mech Eng. 2020;362(2):112790. doi:10.1016/j.cma.2019.112790.